ELSEVIER

Physica D 141 (2000) 19–36

PHYSICA D

www.elsevier.com/locate/physd

The diffusionless Lorenz equations; Shil'nikov bifurcations and reduction to an explicit map

Gerard van der Schrier*, Leo R.M. Maas

Netherlands Institute for Sea Research, PO Box 59, 1790 AB Texel, The Netherlands

Received 15 March 1999; received in revised form 22 November 1999; accepted 3 February 2000
Communicated by A. Doelman

Abstract

A simplified, one-parameter version of the Lorenz model is obtained in the limit of high Rayleigh- and Prandtl-numbers, physically corresponding to diffusionless convection. It is argued that the bifurcation structure of this simplified Lorenz model essentially involves only Shil'nikov bifurcations. An exact solution to this simplified dynamical system is given which serves as the limit for strong forcing and appears to be a new integrable case of the Lorenz equations. For small values of the bifurcation parameter, an approximate, analytical and multipeaked map is obtained which gives successive periods of the pulse-like motion. This map leads to self-similar behaviour in parameter-space.

PACS: 47.20.Bq; 47.20.Ky

Keywords: Lorenz equations; Bifurcation structure; Reduction to a map; Shil'nikov bifurcations

1. Introduction

The Lorenz equations [12], envisaged as a model for convection between parallel plates, have grown into *the* paradigm for chaotic systems. The numerical computations performed by Lorenz showed that solutions are aperiodic and depend sensitively on the initial conditions. This characteristic feature of the solutions can be understood by the observation that the dynamics seem to reduce to the iteration of a one-dimensional map, relating one oscillatory cycle to the next. This map is single-cusped under Lorenz's choice of parameters and resembles the so-called tent map, for which the occurrence of chaos can be firmly established. In another publication [13], a different set of parameters is chosen and Lorenz obtained here a multi-cusped map. However, is it possible to simplify the Lorenz model even further, without losing either its physical basis or its chaotic behaviour? And is it possible to compute this map analytically instead of numerically? The first question only recently attracted attention from a mathematical perspective [19]. The present work gives a physically motivated simplification of the Lorenz equations, reducing it to a one-parameter set called the diffusionless Lorenz equations (DLE), which indeed still possess chaotic behaviour.

* Corresponding author. Tel.: +31-222-369426; fax: +31-222-319674.
E-mail address: schrier@nioz.nl (G. van der Schrier)

0167-2789/00/$ – see front matter
PII: S0167-2789(00)00033-6

Moreover, in relation to the second question, we show here that the dynamics of the DLE can be reduced to an *analytical* map for small values of the remaining parameter R. This map is, similar to the one obtained by Lorenz [13], multi-cusped but, in contrast to this map and the one obtained in [12], written both in implicit and explicit form.

The Lorenz equations model the evolution of coefficients of a severely truncated Fourier series, rudimentarily describing the temperature and streamfunction of fluid between parallel plates, and lacks therefore a direct physical interpretation. However, through a translation and reorientation the equations also represent an energetically closed description of convection in a box in terms of the position of the centre-of-mass (y,z) and the box-averaged angular momentum x. These equations are [14]:

$$\sigma^{-1}\dot{x} = -y - x, \tag{1a}$$

$$\dot{y} = -xz - y, \tag{1b}$$

$$\dot{z} = xy - \mu z + B, \tag{1c}$$

where a dot indicates time t derivative. The linear terms at the right-hand side of (1a) represent buoyancy torque and viscous damping, respectively. The nonlinear and linear terms in Eqs. (1b) and (1c) represent advection and (thermal) diffusion, respectively. The forcing is denoted by B, the flux-Rayleigh number, and is assumed to be spatially homogeneous. With positive B we prescribe a uniform cooling at the top of the box or (equivalently) a uniform heating at its base. The Prandtl number, σ, measures the balance between viscous effects and diffusion, while μ is the ratio of vertical to horizontal diffusion timescales. The stationary equilibria of (1a)–(1c) are

$$(x, y, z) = \left(0, 0, \frac{B}{\mu}\right) \quad \text{and} \quad (x, y, z) = (\pm\sqrt{B-\mu}, \mp\sqrt{B-\mu}, 1),$$

the so-called diffusive and convective equilibria, respectively. Eqs. (1a)–(1c) can be identified with the Lorenz [12] equations by the translation and rescaling: $z \to -z + B/\mu$, $y \to -y$, where Lorenz's parameters σ, r and b equal σ, B/μ and μ, respectively.

The input of energy by the buoyancy forcing is checked by two mechanisms, mechanical friction and diffusion. It turns out that when we assume a balance between forcing and diffusion, by neglecting viscous effects, the convective equilibria cease to exist and only the diffusive equilibrium remains. The scaling which leads to this balance, $(x, y, z, t) \to (x, y/\sigma, z/\sigma, t)$ in the limit $\sigma \to 0$ while $R = \sigma B$ remains finite, invalidates itself since physically unacceptable behaviour is generated: in the absence of mechanical friction the angular momentum increases indefinitely, earlier noted by Kolář and Gumbs [10]. If, on the other hand, a balance is assumed between forcing and viscosity, the diffusive equilibrium ceases to exist. This situation is the most interesting case of the two and in the remainder of this study we will limit ourselves to the corresponding parameter regime. Rescaling (1a)–(1c): $(x, y, z) \to \sigma(x, y, z)$ and $t \to t/\sigma$ and considering the distinguished limit $\sigma, B \to \infty$, while $R \equiv B/\sigma^2$ remains finite, (1a)–(1c) reduce to

$$\dot{x} = -y - x, \tag{2a}$$

$$\dot{y} = -xz, \tag{2b}$$

$$\dot{z} = xy + R. \tag{2c}$$

The single-parameter equations (2a)–(2c) are referred to in the remainder of this study as the DLE. System (2a)–(2c) popped up (with $R = 1$) in a search for chaotic low-order systems of the form $\dot{\mathbf{x}} = F(\mathbf{x})$ with $F(\mathbf{x})$ algebraically as simple as possible [19, Case B]. The present work gives a physical motivation for studying (2a)–(2c) for $R \in \mathbb{R}^+$.

In case the forcing is weak ($0 < R \ll 1$), we can approximate the (possibly chaotic) dynamics by an explicit analytical map. An elaborate implicit map was derived, under more general circumstances, by Fowler and McGuinness [4,5] for the full Lorenz equations. We believe, however, that the present derivation may serve as a didactical purpose in that it is much simpler to be established owing to the simplified nature of the DLE. It will also lead to an *explicit* map and might hence be suitable as a method to be exploited in different circumstances too. Moreover, the diffusive equilibrium (in Fowler and McGuinness' map still a stationary point) fulfils a special role in the dynamics of their map, discussed in Section 4. We will show here, however, that an analytical map based on the DLE, where the diffusive equilibrium ceases to be a stationary point, still reproduces the essentials of the Fowler and McGuinness map. This study comments on the role of the origin as a stationary point in the Lorenz equations and the homoclinic orbits associated with it.

The complicated behaviour of the model in this parameter regime finds its origin in Shil'nikov bifurcations, a special homo- or heteroclinic bifurcation [6,11,12]. The dynamical structure of the model is sketched in Section 2 and its dynamics, in the regime of weak forcing, can be reduced to the iteration of an explicit map reproducing certain aspects obtained by numerical integration (Section 3). A discussion of these results in the light of earlier work is given in Section 4.

2. Dynamical structure

The dynamical system under consideration models convective processes in a rectangular box in terms of the basin-averaged angular momentum and density gradients [14]. When allowing for motion in a vertical plane only, the dynamical state is described by the angular momentum in this plane, x, the lateral density gradient, y, and the vertical density gradient, z. A much more revealing interpretation of the latter two variables is as giving the horizontal and vertical position of the centre-of-mass in this plane (with respect to the geometric centre). The motion of the centre-of-mass determined by the combined effects of buoyancy input and friction can be depicted as follows: the forcing tends to raise the centre-of-mass, eventually above the geometric centre, while the overturning, conserving the distance between centre-of-mass and geometric centre, transfers it below the geometric centre again. This process can be compared to the motion of an equivalent pendulum. This pendulum can raise its centre-of-mass beyond the pivot, and when not exactly in its upright position, will subsequently swing back again because of gravity, giving rise to (damped) oscillations. In Section 3 we will refer to this equivalent pendulum wherever applicable.

Just as the Lorenz equations, the DLE are invariant under the symmetry

$$(x, y, z) \to (-x, -y, z), \tag{3}$$

but have only two steady states:

$$C^{\pm} = (\pm\sqrt{R}, \mp\sqrt{R}, 0). \tag{4}$$

The eigenvalues are the roots of the characteristic equation, which is obtained by linear stability analysis around solution (4):

$$\lambda^3 + \lambda^2 + \lambda R + 2R = 0.$$

It can be verified that if $R > 0$, equilibria (4) are saddle-foci with one real linearized eigenvalue, $-\lambda_1$, and a pair of complex conjugate linearized eigenvalues, $\lambda_2 \pm \mathrm{i}\omega$. The ratio $\delta \equiv \lambda_2/\lambda_1$ is always smaller than 1 provided $R > 0$. (In fact, for $R > 0$, we have $0 < \delta < \frac{1}{4}$.) With this condition satisfied, and in the presence of a homoclinic connection, we have the Shil'nikov phenomenon [6,11,22].

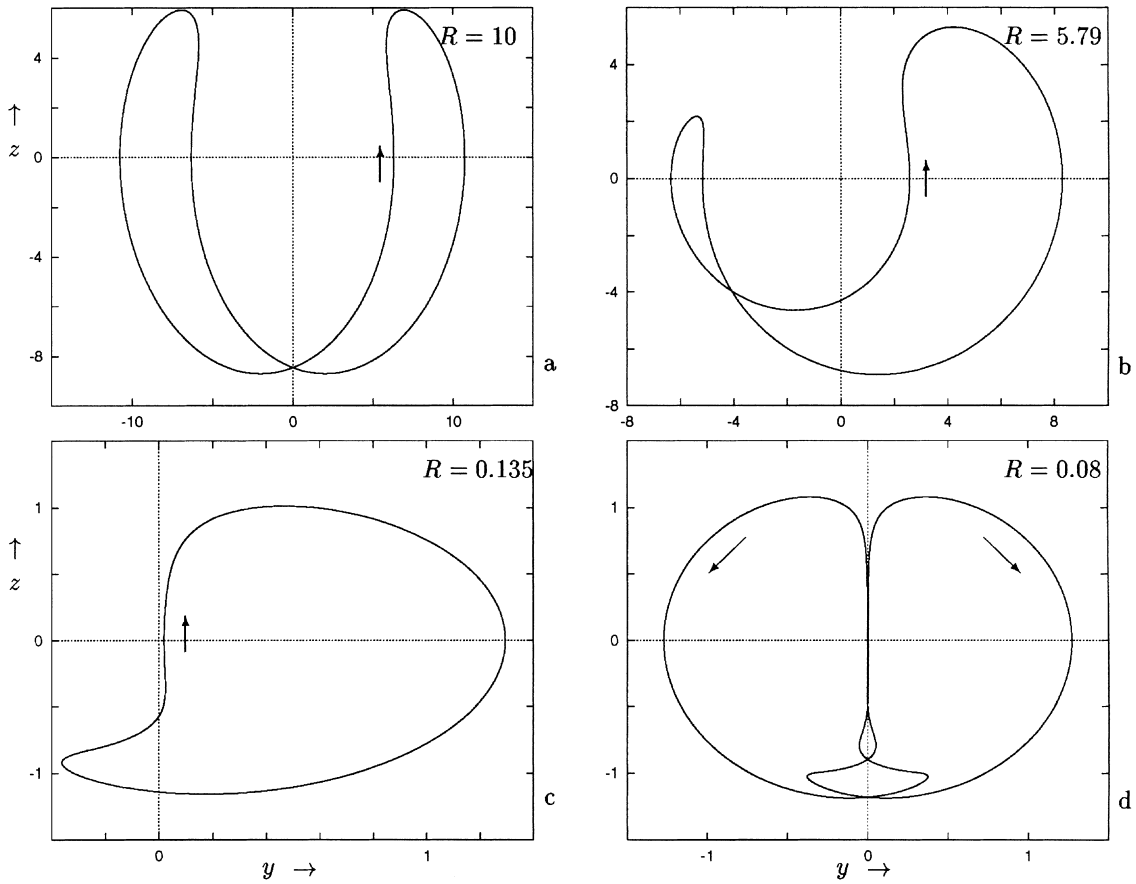

Fig. 1. Phase-portraits of the flow as determined by (2a)–(2c) for four different values of parameter R. The figures for $R = 5.79$ and $R = 0.135$ are one of the two coexisting mirror-imaged solutions situated on the same branch of Fig. 2b. Variables y and z denote the lateral and vertical position of the centre-of-mass with respect to the geometric centre, respectively. The arrows give the direction of the flow.

Characteristic motion of system (2a)–(2c) at $R = 10$ is pictured in Fig. 1a. Variable z grows and turns positive due to the forcing while y initiates its growth and triggers a sudden increase in x (not shown). This periodic solution can be followed numerically through parameter space with AUTO [1]. Decreasing R, we obtain a spiral-shaped curve in the amplitude–parameter space (Fig. 2a). Each point in this branch represents a periodic solution. This branch extends towards positive infinity, and for smaller values of R, winds itself up to disappear at the locus in a heteroclinic bifurcation at $R \approx 1.05$, identified numerically. The periodic solutions on this branch become increasingly similar to a heteroclinic orbit and we will refer to this branch as the symmetrical principal branch (SPB) since its solutions are invariant to the symmetry (3) and since its locus in parameter space is the simplest heteroclinic connection found.

A periodic orbit as found on the SPB has been extensively discussed by Glendinning and Sparrow [6]. It suffices to mention that the SPB, followed in parameter space from positive infinity to its locus, loses its stability at p_1 near $R = 6.75$ and regains it at p_2 near $R = 0.23$ in symmetry breaking bifurcations. At both these bifurcations, two branches of mirror-imaged asymmetric periodic orbits emerge (Fig. 1b and c) and each branch terminates at the loci in a homoclinic bifurcation (Fig. 2b and c). The branch that emerges from the SPB at p_1 loses stability by a period-doubling cascade starting at d_1 ($R \approx 5.44$), leading to chaotic motion. An inverse cascade restabilizes

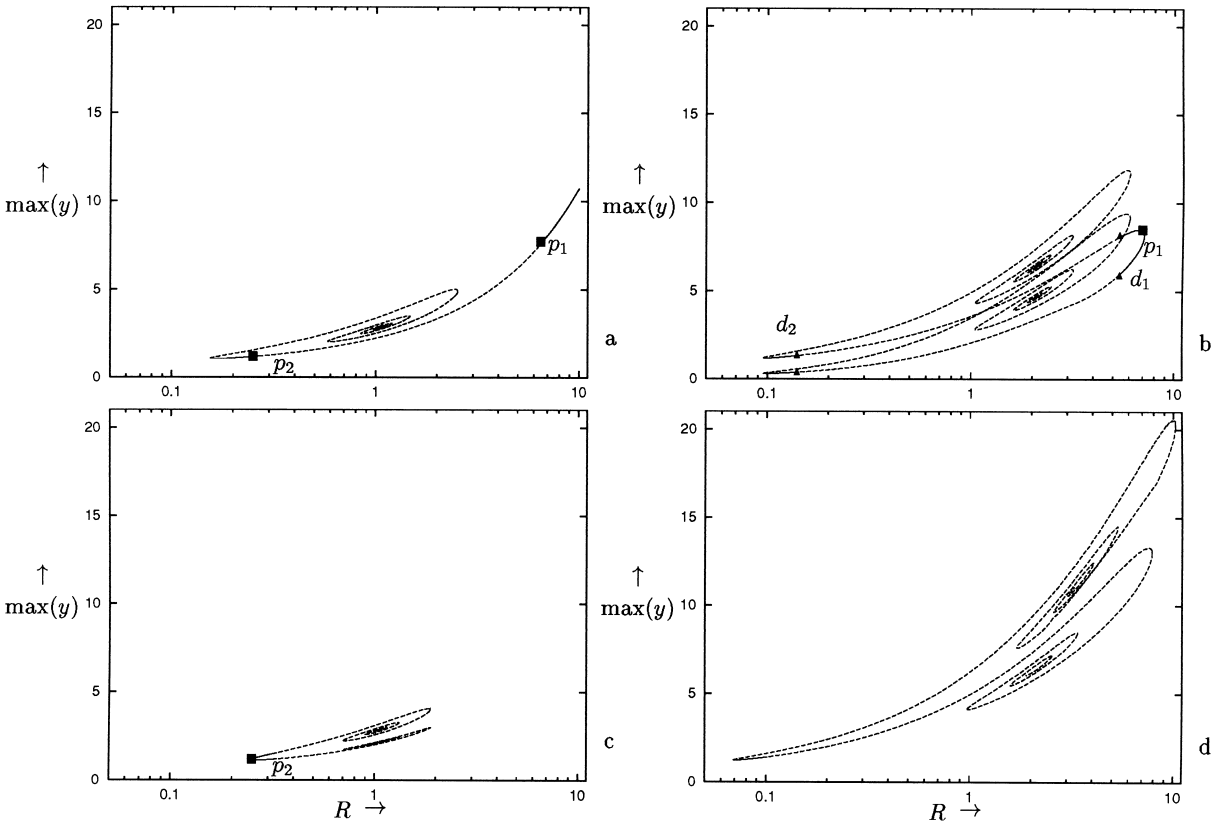

Fig. 2. The bifurcation diagrams for the parameter R: (a) symmetrical principal branch (SPB); (b) periodic solutions which branch off at p_1; and (c) periodic solutions which branch off at p_2; (d) distinct branch having no connection in parameter space to the principal orbit of Fig. 2a. The symmetry breaking bifurcations p_1, p_2 have been indicated by solid squares, while the period-doubling bifurcations d_1, d_2 are indicated by solid triangles.

the asymmetric orbit, and the periodic solution which is created by the first period doubling at d_1 can be followed through the chaotic regime and it is this orbit which restabilizes the original asymmetric orbit at d_2. Other periodic orbits which are created in period-doubling bifurcations can approach homoclinicity themselves. The bifurcations p_1 and d_1, the period-doubling cascades and the subsequent chaotic motion is, among other dynamical behaviour, retrieved in a numerical computation of a Poincaré plot (Fig. 3) and a plot of the Lyapunov exponents (Fig. 4). The locations of the bifurcations as computed with AUTO and by computing the Poincaré plot and Lyapunov exponents match exactly.

The structures of Fig. 2a–c do not extend over the whole R-parameter range. Given the negative divergence of (2a)–(2c) ($\nabla \cdot (\dot{x}, \dot{y}, \dot{z}) = -1$) the flow must have at least one attractor below the minimum R reached, be it a stationary point, a periodic orbit or a strange invariant set [8]. For $R = 0.08$ we find the motion presented in Fig. 1d which is characterized by z growing slowly to positive values until it quickly turns negative again, and the branch on which this solution is found is given in Fig. 2d. We have not found a connection between this structure and the SPB or any orbit bifurcating from the latter. Parameter space for still smaller (positive) values of R is filled with an infinite sequence of such detached orbits, of which Fig. 2d presents the outermost limit. This will be substantiated in Section 3.2.2. Each of these orbits will have their own bifurcations.

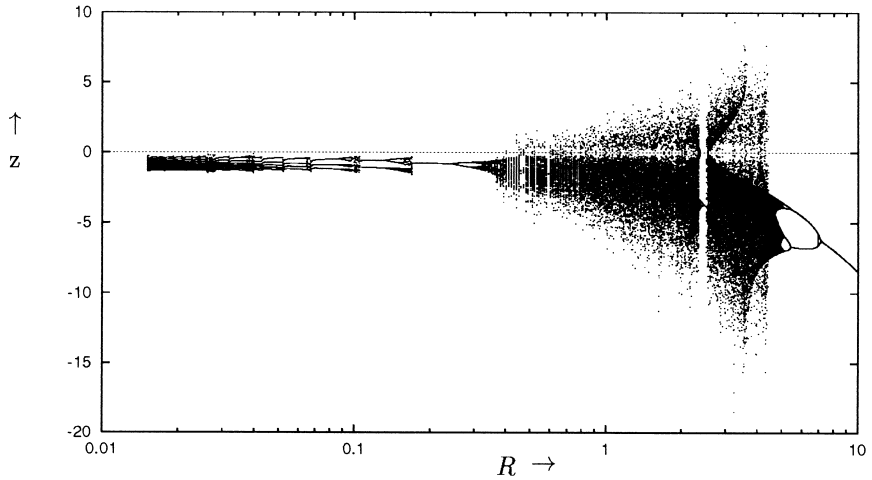

Fig. 3. Numerically determined Poincaré section at $y = 0$ versus R. The behaviour in parameter space has been investigated by numerically integrating Eqs. (2a)–(2c) from $R = 10$ downwards, and each run is initialized in the endpoint of the previous run.

An analogy that forces itself upon us when describing the bifurcation structure of system (2a)–(2c) is the following. The SPB is a tree with an (infinite) number of ever bifurcating branches. But, parameter space is filled with *other* such trees, together forming a complete 'forest' of equilibria.

3. Approximate solutions

3.1. Strong forcing

Numerically computed motion for $R \gg 1$ is given in Fig. 1a ($R = 10$). An asymptotically correct analytic description of motion for $R \gg 1$ is given in Appendix A (which is simpler than Robbins's [16] or Shimizu's [17]

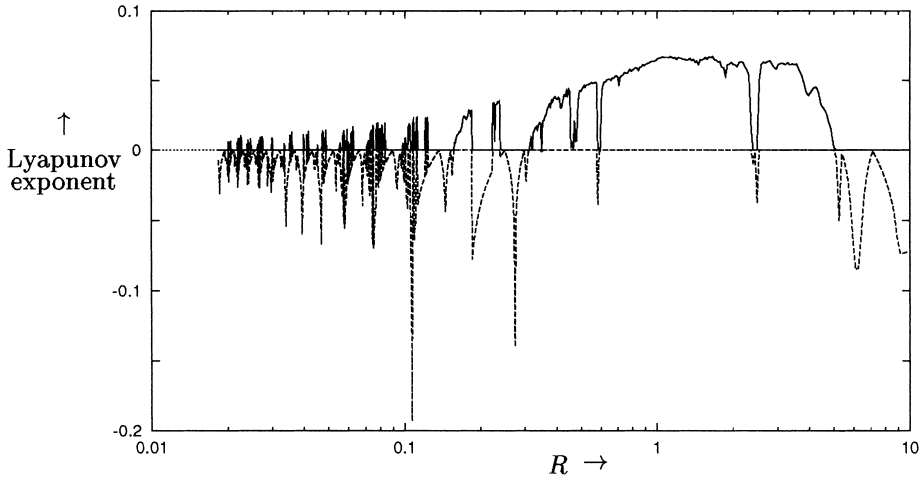

Fig. 4. The two largest Lyapunov exponents (solid and dashed, respectively) versus R as determined by numerical integration of Eqs. (2a)–(2c). A positive and a zero Lyapunov exponent indicates chaotic motion, two zero Lyapunov exponents indicate a bifurcation and a zero and a negative Lyapunov exponent indicates regular periodic motion. Each run is initialized near one of the static equilibria.

solutions due to the simplified nature of the DLE). However, an *exact* solution can also be obtained in the limit $R \to \infty$. Rescale (2b) and (2c) with

$$(x, y, z, t) \to (R^{1/3}x, R^{2/3}y, R^{2/3}z, R^{-1/3}t),$$

and take the limit $R \to \infty$. This results in

$$\dot{x} = -y, \tag{5a}$$

$$\dot{y} = -xz, \tag{5b}$$

$$\dot{z} = xy + 1. \tag{5c}$$

We now have $\frac{1}{2}x^2 + z - t = c$. The constant of integration c can be absorbed in time and thus, without loss of generality, be set equal to zero. This relation together with (5a) and (5b) yields

$$\frac{\mathrm{d}^2x}{\mathrm{d}t^2} = x\left(t - \frac{x^2}{2}\right),$$

which is with one further substitution, $x = 2\mathrm{i}\xi$, identical to

$$\frac{\mathrm{d}^2\xi}{\mathrm{d}t^2} = 2\xi^3 + t\xi, \tag{6}$$

an equation solved by the second Painlevé transcendent [9, p. 345] that behaves asymptotically like elliptic functions [20] (see Appendix A). This solution should serve as the limit for $R \to \infty$ and appears to be a new integrable case of the Lorenz equations, not listed in Tabor [21].

3.2. Weak forcing

Numerical experiments with $0 < R \ll 1$ demonstrate that quasi-periodic, attracting states exist where each cycle is characterized by alternating phases of fast and slow motion. The slow motion can be associated with the equivalent pendulum hanging nearly vertical in a stable position and the forcing slowly raising it. It then passes the geometric centre, thus becoming unstable. However, it takes time for the instability to grow, during which time the centre-of-mass keeps rising, until it suddenly and violently overturns; the fast part of the cycle. During this fast part, the input of energy is negligible, and thus the distance to the geometric centre is conserved. Eventually the pendulum approaches a stable position, the oscillations are quickly damped and it is soon nearly vertical ($y \simeq 0$) in its stable position again (Fig. 5). The closer the pendulum is to the vertical, the longer it takes for the instability to grow. The inequality in length of subsequent cycles and the overturning *sense* of the next cycle reflect this sensitivity.

A description of the dynamics of a cycle can be obtained as follows. During the slow phase, the pendulum is always very close to the vertical and smoothly rising and thus the distance, $r = (y^2 + z^2)^{1/2}$, is first linearly decreasing and then (after passing the geometric centre) a linearly increasing function of time. In the fast phase, r remains constant (Fig. 5b). This suggests a polar co-ordinate representation of the centre-of-mass location: $y = -r\sin\theta$ and $z = -r\cos\theta$, and Eqs. (2a)–(2c) change into

$$\dot{x} = r\sin\theta - x, \tag{7a}$$

$$\dot{r} = -R\cos\theta, \tag{7b}$$

$$\dot{\theta} = -x + \frac{R}{r}\sin\theta. \tag{7c}$$

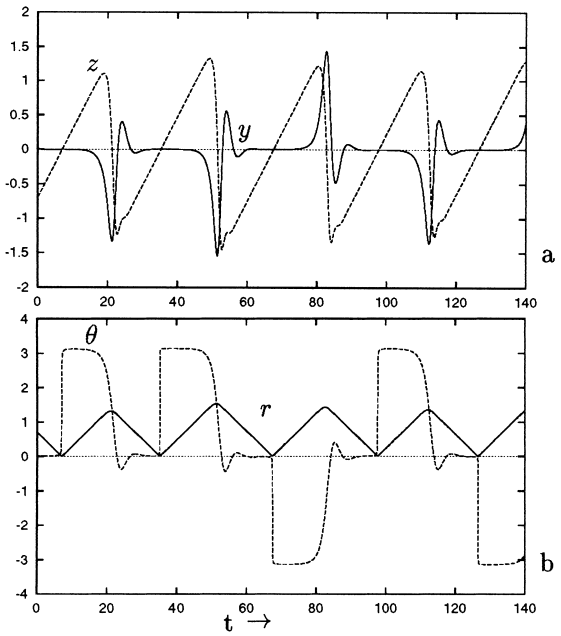

Fig. 5. Time evolution of the lateral and vertical density gradients (i.e. horizontal and vertical position of the centre-of-mass) y and z (a) and the radius r and phase angle θ in the polar co-ordinate representation (b) for $R = 0.1$. This is a numerical integration of the DLE (2a)–(2c).

On the slow time Rt, the solutions are

$$x = 0, \qquad \theta = 0, \qquad r = -Rt - c_1, \tag{8a}$$

$$x = 0, \qquad \theta = \pi, \qquad r = Rt + c_2, \tag{8b}$$

which can be associated with the phases where r decreases and increases in time, respectively. On the fast timescale t, we have, for $r \gg 0$,

$$\dot{x} = r \sin\theta - x, \tag{9a}$$

$$\dot{r} = 0, \tag{9b}$$

$$\dot{\theta} = -x. \tag{9c}$$

Substituting (9c) in (9a) gives

$$\ddot{\theta} + \dot{\theta} + r(Rt) \sin\theta = 0. \tag{10}$$

Because of the nearly vertical position of the pendulum reflected in solutions (8a) and (8b) we approximate $\sin\theta$ by $\pm\theta$ and substitute the solution for r (Eqs. (8a) and (8b)). A further substitution, $\theta = \mathrm{e}^{-t/2}\,\tilde{\theta}$, transforms Eq. (10) into

$$\ddot{\tilde{\theta}} - (Rt + c_{2,1} + \tfrac{1}{4})\tilde{\theta} = 0. \tag{11}$$

Now, rescale time into $\tau = R^{1/3}(t + c_{2,1}R^{-1} + \frac{1}{4}R^{-1})$ and Eq. (11) reduces to the Airy differential equation

$$\ddot{\tilde{\theta}} - \tau\tilde{\theta} = 0. \tag{12}$$

A general solution for θ is

$$\theta = \mathrm{e}^{-t/2}[\alpha\,\mathrm{Ai}(R^{1/3}t + R^{-2/3}c_{2,1} + \tfrac{1}{4}R^{-2/3}) + \beta\,\mathrm{Bi}(R^{1/3}t + R^{-2/3}c_{2,1} + \tfrac{1}{4}R^{-2/3})] + (\pi, 0). \tag{13}$$

The heart of the nonlinear DLE (for $0 < R \ll 1$) is thus formed by a solvable *linear*, second-order differential equation, whose solution applies over a time span that has been left *indeterminate*. The complete approximate solution requires the determination of this time span, here referred to as its 'period' (without assuming a priori that the motion is strictly periodic). The nonlinearity of the DLE is thus retrieved in a map that relates the time span (period) of one cycle to that of the next. This is determined by matching θ for r *increasing* in time ($\theta \approx \pi$) to θ for r *decreasing* in time ($\theta \approx 0$), subscripted with i and d, respectively. For $r = 0$ at the time-origin $t = 0$, thus $c_2 = 0$,

$$\theta_\mathrm{i} = \mathrm{e}^{-t/2}[\alpha_\mathrm{i}\,\mathrm{Ai}(R^{1/3}t + \tfrac{1}{4}R^{-2/3}) + \beta_\mathrm{i}\,\mathrm{Bi}(R^{1/3}t + \tfrac{1}{4}R^{-2/3})] - s\pi \tag{14}$$

for $t \in [0, TR^{-1}]$ with $s \equiv \mathrm{sgn}(\beta_i)$, and for the decreasing part we choose $r = 0$ when $t = 2TR^{-1}$ thus $c_1 = -2T$,

$$\theta_\mathrm{d} = \mathrm{e}^{-t/2+T/R}[\alpha_\mathrm{d}\,\mathrm{Ai}(R^{1/3}t + (\tfrac{1}{4} - 2T)R^{-2/3}) + \beta_\mathrm{d}\,\mathrm{Bi}(R^{1/3}t + (\tfrac{1}{4} - 2T)R^{-2/3})] \tag{15}$$

for $t \in [TR^{-1}, 2TR^{-1}]$. With TR^{-1} half the period of the motion remains to be determined. The information contained in the coefficient α_i is lost as the motion veers to a slow manifold, since the Airy function Ai becomes exponentially small for large positive argument, and θ_i is determined almost completely by the monotonically increasing Bi-function. In particular, the sign of β_i will determine whether θ_i will increase or decrease. The simplest way to match (14) and (15) is by defining (half) the period of a cycle T *implicitly*, by requiring continuity at $\theta(t) = -\frac{1}{2}s\pi$ of $\theta(t)$ and $\dot{\theta}(t)$:

$$\lim_{t\uparrow T/R} \theta_\mathrm{i} = -\tfrac{1}{2}s\pi, \tag{16a}$$

$$\lim_{t\uparrow T/R} \theta_\mathrm{i} = \lim_{t\downarrow T/R} \theta_\mathrm{d}, \tag{16b}$$

$$\lim_{t\uparrow T/R} \dot{\theta}_\mathrm{i} = \lim_{t\downarrow T/R} \dot{\theta}_\mathrm{d}. \tag{16c}$$

By requiring continuity of x at the transition of one cycle to the next, it can be established that despite the π-jump in the phase angle $\theta = \tan^{-1}(y/z)$, the values of α_d and β_d are conserved as r passes the geometric centre. Thus

$$\alpha_\mathrm{d} \to \alpha_\mathrm{i} \quad \text{and} \quad \beta_\mathrm{d} \to \beta_\mathrm{i}.$$

3.2.1. Approximate analytical map of the DLE

The matching conditions (16a)–(16c) provide three equations which can be seen as a parametric relation with parameter T. A given T is related to the coefficient β_i by Eq. (16a):

$$\beta_\mathrm{i}\,\mathrm{Bi}(R^{-2/3}(T + \tfrac{1}{4})) = \tfrac{1}{2}s\pi\,\mathrm{e}^{T/2R}. \tag{17a}$$

Eq. (16b) and (16c) together determine the coefficients α_d and β_d of the next phase of the cycle as a function of T and $\beta_\mathrm{i}(T)$ by solving

$$\mathrm{e}^{T/R}\begin{pmatrix} \mathrm{Ai}(\tau^-) & \mathrm{Bi}(\tau^-) \\ -\frac{1}{2}\mathrm{Ai}(\tau^-) + R^{1/3}\,\mathrm{Ai}'(\tau^-) & -\frac{1}{2}\mathrm{Bi}(\tau^-) + R^{1/3}\,\mathrm{Bi}'(\tau^-) \end{pmatrix}\begin{pmatrix} \alpha_\mathrm{d} \\ \beta_\mathrm{d} \end{pmatrix} = \begin{pmatrix} \beta_\mathrm{i}\,\mathrm{Bi}(\tau^+) - s\pi\,\mathrm{e}^{T/2R} \\ -\frac{1}{2}\beta_\mathrm{i}\,\mathrm{Bi}(\tau^+) + R^{1/3}\beta_\mathrm{i}\,\mathrm{Bi}'(\tau^+) \end{pmatrix} \tag{17b}$$

with

$$\tau^{\pm} = R^{-2/3}(\tfrac{1}{4} \pm T) \tag{17c}$$

introduced for notational convenience. From β_{d} in turn, the period T^* of the next cycle can be determined, thus implicitly yielding a map $T^*(T)$ by inverting (17a), and replacing β_{i} by $\beta_{\mathrm{d}}(T)$.

An approximate explicit map can be obtained as follows. First, relate the period T to the coefficient β_{i} (17a):

$$\beta_{\mathrm{i}} = \frac{s(\pi/2)\,\mathrm{e}^{T/2R}}{\mathrm{Bi}(\tau^+)}.$$

Second, relate β_{i} and T to β_{d}, as given by Eq. (17a) and reduce this to

$$\beta_{\mathrm{d}} = -\frac{s}{2}\frac{\pi^2}{R^{1/3}}\,\mathrm{e}^{-T/2R}\mathrm{Ai}(\tau^-)\left[1 - \frac{R^{1/3}\,\mathrm{Ai}'(\tau^-)}{\mathrm{Ai}(\tau^-)} - \frac{R^{1/3}\,\mathrm{Bi}'(\tau^+)}{\mathrm{Bi}(\tau^+)}\right], \tag{18}$$

using that the Wronskian of $(\mathrm{Ai}, \mathrm{Bi}) = \pi^{-1}$. Finally, solve Eq. (17a) for the period of the next cycle by replacing T by T^*. Substituting the asymptotic representation of the Bi-function (valid for large positive argument),

$$\mathrm{Bi}(x) \approx \frac{\mathrm{e}^{2x^{3/2}/3}}{\sqrt{\pi\sqrt{x}}}$$

in (17a), subsequently taking natural logarithms on both sides and subtracting $1/8$ results in

$$\tfrac{2}{3}(T^* + \tfrac{1}{4})^{3/2} - \tfrac{1}{2}T^* - \tfrac{1}{4}R\log[T^* + \tfrac{1}{4}] - \tfrac{1}{8} = R\log\left[\frac{\pi^{3/2}}{R^{1/6}\beta_{\mathrm{i}}}\frac{s}{2}\right] - \tfrac{1}{8} \equiv p(T, R). \tag{19}$$

By using the conservation of β_{i} into the next phase of the cycle, $\beta_{\mathrm{i}} = \beta_{\mathrm{d}}$, and substituting

$$(T^* + \tfrac{1}{4})^{1/2} \equiv \eta, \tag{20}$$

Eq. (19) reduces to

$$\tfrac{2}{3}\eta^3 - \tfrac{1}{2}\eta^2 - \tfrac{1}{4}R\log\eta^2 = p. \tag{21}$$

With (18), p, defined in the right-hand side of (19), reads

$$p(T, R) = \tfrac{1}{2}T - \tfrac{1}{8} - R\log\left[\frac{\pi^{1/2}}{R^{1/6}}\left|\mathrm{Ai}(\tau^-)\left\{1 - \frac{R^{1/3}\,\mathrm{Ai}'(\tau^-)}{\mathrm{Ai}(\tau^-)} - \frac{R^{1/3}\,\mathrm{Bi}'(\tau^+)}{\mathrm{Bi}(\tau^+)}\right\}\right|\right]. \tag{22}$$

The absolute sign in the logarithm results from $\beta_{\mathrm{i}} = s|\beta_{\mathrm{i}}|$. In the case of weak forcing, $0 < R \ll 1$, we assume that $\eta = \eta_0 + R\eta_1 + \mathrm{O}(R^2)$, and in zeroth order, Eq. (21) reduces to a third order polynomial

$$\tfrac{2}{3}\eta_0^3 - \tfrac{1}{2}\eta_0^2 = p. \tag{23a}$$

The only real positive root of (23a) is (for p>0)

$$\eta_0 = \tfrac{1}{2}\cosh\left(\tfrac{1}{3}\phi\right) + \tfrac{1}{4}, \tag{23b}$$

where

$$\phi = \mathrm{arccosh}(|48p(T, R) + 1|), \tag{23c}$$

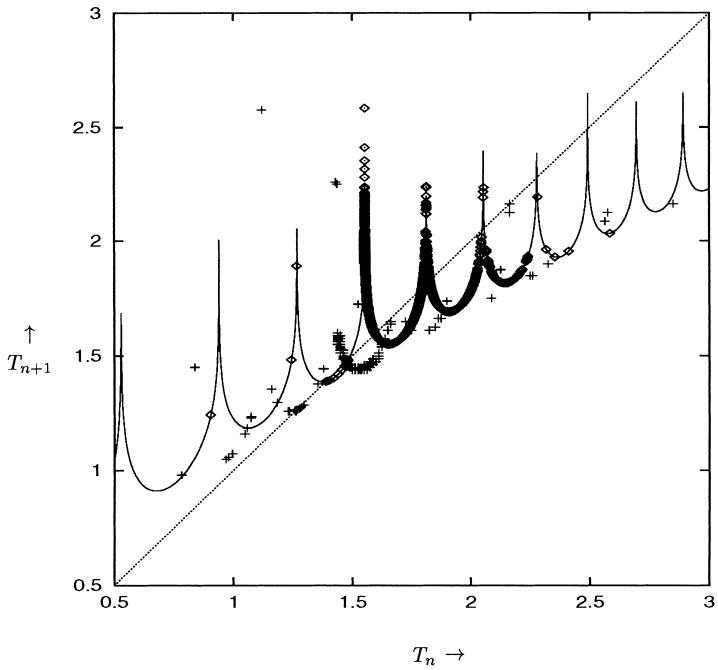

Fig. 6. Results from maps of successive periods of the motion for $R = 0.1$. The implicit map (17a)–(17c) ($\diamond$) and its explicit functional approximation (24) (solid curve) are compared with results from the direct numerical integration of the DLE (+). The dotted line is the bisector. The height of the cusps is infinite.

and its first order correction is

$$\eta_1 = \frac{\frac{1}{4}\log(\eta_0^2)}{2\eta_0^2 - \eta_0}. \tag{23d}$$

Concluding, with the above formulas, the approximate *explicit* map is given by

$$T^*(T) = [\eta_0(T) + R\eta_1(\eta_0(T))]^2 - \tfrac{1}{4}. \tag{24}$$

In Fig. 6, the map, given by Eq. (17a)–(17c), for two different starting values of T, and its functional dependence, given by Eq. (24), correct up to $O(R)$ are plotted for $R = 0.1$. A regular period-one solution is found, culminating at $T \sim 1.4$ as well as chaotic motion ($T > 1.5$) is found for different initial conditions. The explicit map's functional dependence approximates the implicit map itself accurately, even for this relatively large value of the small parameter, and it can be computed far more efficiently.

The fixed points of the map, located at the intersections with $T_{n+1} = T_n$, correspond to limit cycles of the orbit. These are stable if $|\mathrm{d}T_{n+1}/\mathrm{d}T_n| < 1$ and unstable otherwise. The map features an infinity of cusps implying the existence of an infinity of fixed points, of which the majority are unstable. The position of the cusps of the map are situated at the zeros of β_d (18):

$$\mathrm{Ai}(\tau^-)\left\{1 - \frac{R^{1/3}\,\mathrm{Ai}'(\tau^-)}{\mathrm{Ai}(\tau)} - \frac{R^{1/3}\,\mathrm{Bi}'(\tau^+)}{\mathrm{Bi}(\tau^+)}\right\} = 0, \tag{25}$$

and with (21) and (22), it can be established that the cusps have infinite height. The position of the envelope of the map is, in an approximate sense, determined by Eqs. (21), with terms of O(R) neglected,

$$\tfrac{2}{3}\eta^3 - \tfrac{1}{2}\eta^2 = \tfrac{1}{2}T - \tfrac{1}{8}. \tag{26}$$

As R increases, the location of the cusps shifts to higher values of T, the cusp spacing increases while the envelope remains constant. This has the effect that a stable period-one limit cycle will double its period successively before becoming chaotic. A new trough of the map will intersect the bisector, and a new pair of fixed points will emerge in a tangent bifurcation, one stable, one unstable.

This sequence of events as R is increased, corresponding to the emergence of a new pair of solutions in a tangent bifurcation, can be related to the bifurcation diagram in Fig. 2. Starting, e.g. on the stable limit cycle on the left extreme of the structure in Fig. 2b, and increasing R, the limit cycle loses its stability due to the period-doubling bifurcation d_2. The bifurcated branch will again bifurcate (not shown) when R increases and by now, the saddle-node bifurcation at the left extreme of the structure in Fig. 2a, is passed and a new pair of solutions emerges.

We have iterated the implicit map (17a)–(17c) as a function of the only control variable R (Fig. 7). Multiple windows, like that obtained by direct numerical integration of the DLE (Fig. 3) or as expressed by the Lyapunov exponent (Fig. 4) are retrieved. For some values of R, iteration of the implicit map showed coexisting equilibria and the hysteresis, earlier shown by Fowler and McGuiness [5], is demonstrated. A lower bound to the period (of about 1.3534...) is evident in Fig. 7, very close to the intersection of the bisector $T^* = T$ with the envelope at $T_\mathrm{p} \approx 1.3529$. Finally, Fig. 7 bears a strong suggestion of self-similarity between windows that will be considered in Section 3.2.3.

3.2.2. Map compared with direct integrations

A succession of periods is computed by direct numerical integration of Eqs. (2a)–(2c) and by iteration of the implicit map (17a)–(17c). The envelope of the curve produced by the map approximates the one obtained by the numerical integration (Fig. 6). The cusp-spacing of both curves is very similar, but the locations of the map's cusps are not correct. It seems that the cusps and the troughs of the map are located at, respectively, the troughs and the cusps obtained by numerical integration! This feature is independent of the parameter; it does not seem to be related to the asymptotics of the map. As the parameter is decreased, the analytical map and the direct numerical integrations become more alike, with the exception of the location of the cusps and troughs. Due to this inaccuracy, the periods predicted by the map will be overestimated and the bifurcations predicted by the map will be slightly offset to the left.

Curiously, Fowler and McGuinness [4] encountered similar problems, in spite of the fact that their method of obtaining the map differs from ours. In their paper they remark that the cusp locations were better predicted using the zeros of Ai$'$ rather than Ai as suggested by their analysis. This suggests that in their map the cusps and troughs are also located at, respectively, the troughs and cusps as produced by direct numerical integrations.

We remain puzzled as to the immediate cause of the discrepancy between numerical and analytical results with respect to the positioning of the cusps and troughs in map (24). A likely candidate for this cause may be an approximation made to reach Eq. (13). We approximated $\sin\theta$ with the sawtooth $\pm\theta$, which is only valid for $\theta \approx (0, \pi)$, but the approximation remains in use up till $\theta = \pm\frac{1}{2}\pi$. The resemblance of the analytical map with the direct numerical integrations may be improved by constructing an internal boundary layer around $\theta = \pm\frac{1}{2}\pi$. Attempts to do so proved futile on the one hand and sacrificed the simplicity of the map on the other hand.

3.2.3. Self-similarity of the map

The computation of the map of the DLE (Fig. 7) as a function of the parameter R strongly suggest a self-similarity in the DLE for small values of R and this is investigated with the explicit map (24). The intersection point of envelope

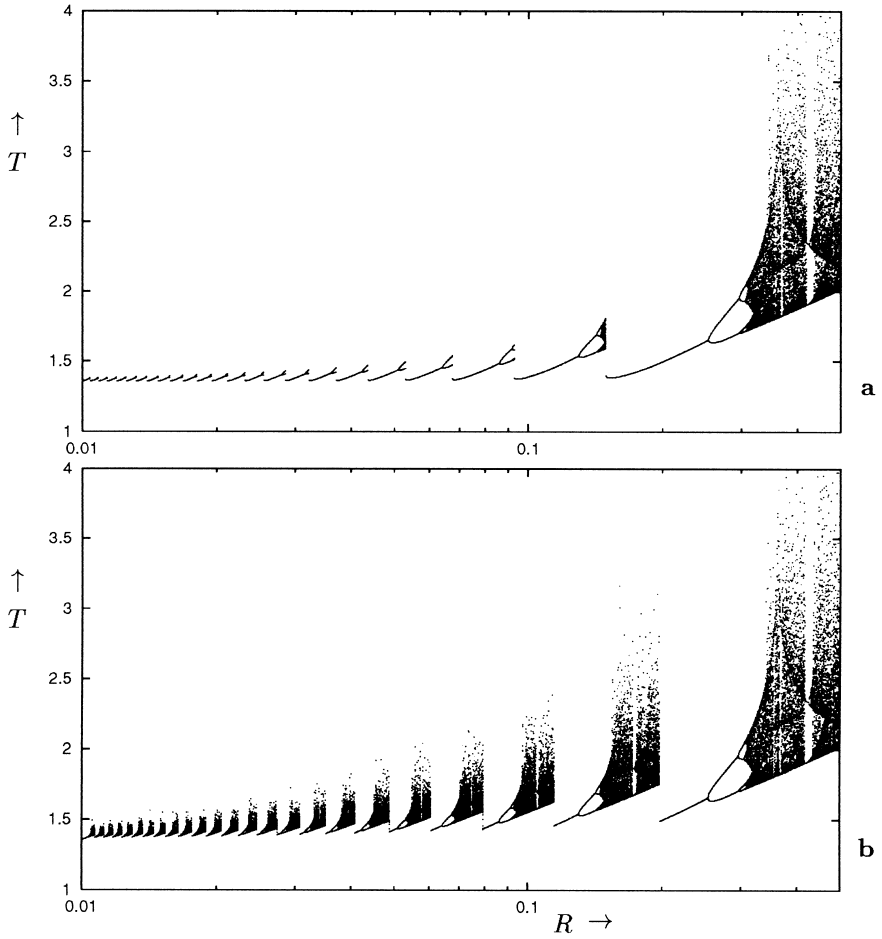

Fig. 7. Bifurcation diagram as computed with the implicit map (17a)–(17c). The starting point for each run was the endpoint of the previous run and (a) was constructed from $R = 0.5$ downwards, while (b) was constructed from $R = 0.01$ upwards.

and bisector, point T_p, plays a pivotal role in the self-similarity, as its position is, up to $O(R)$, independent of the parameter R. The positions of the cusps, however, shift to smaller values of T while the distance between individual cusps decreases for a decreasing parameter. Self-similarity with parameter values R_1 and R_2, is obtained when identical results are produced, up to a multiplicative scaling factor α. Under this scaling factor, the cusps should be mapped upon themselves. This observation provides the basis to compute R_2 and α given R_1.

With the asymptotic representations of the Airy functions Ai, Bi and their derivatives Ai′, Bi′, we have

$$\frac{\mathrm{Bi}'(\tau^+)}{\mathrm{Bi}(\tau^+)} = \left(\frac{T+\frac{1}{4}}{R^{2/3}}\right)^{1/2}(1+\mathrm{O}(R))$$

and

$$\mathrm{Ai}(\tau^-) = \frac{1}{\sqrt{\pi}}\left(\frac{R^{2/3}}{T-\frac{1}{4}}\right)^{1/4}\sin(\zeta+\tfrac{1}{4}\pi), \qquad \mathrm{Ai}'(\tau^-) = \frac{-1}{\sqrt{\pi}}\left(\frac{T-\frac{1}{4}}{R^{2/3}}\right)^{1/4}\cos(\zeta+\tfrac{1}{4}\pi)(1+\mathrm{O}(R))$$

with $\zeta = \frac{2}{3}(T-\frac{1}{4})^{3/2}R^{-1}$. These approximations are valid for $T > \frac{1}{4}$ and $0 < R \ll 1$.

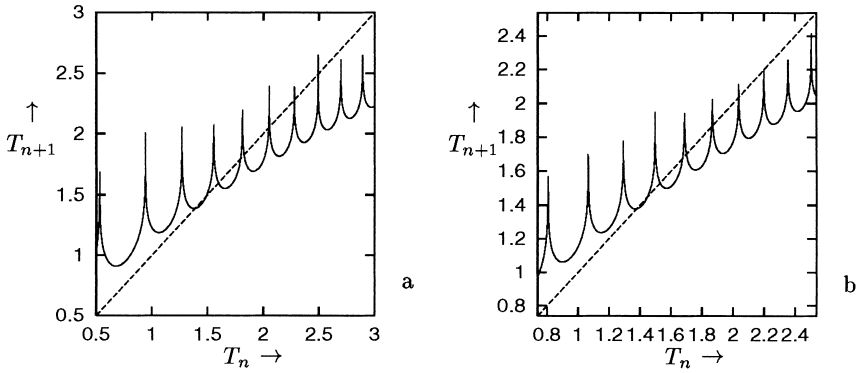

Fig. 8. A demonstration of the self-similarity of map (24) for small values of the parameter R: (a) curve as found with $R = 0.1$; (b) computed with $R = 0.07102$ and a scaling factor $\alpha = 0.71935$. The dotted line is the bisector.

The position of the cusps in the map, given by Eq. (25), can now be simplified to

$$A(T)\cos(\zeta + \tfrac{1}{4}\pi - \phi) = 0, \tag{27}$$

with $\tan\phi = \{1-(T+\frac{1}{4})^{1/2}\}/(T-\frac{1}{4})^{1/2}$ and $A(T) = 2^{1/2}((T+\frac{1}{4})^{1/2} - \frac{1}{2})$, a (positive definite) amplitude. The location of the cusps is given by the zero's of the cosine function:

$$\tfrac{2}{3}(T-\tfrac{1}{4})^{3/2}R^{-1} - \tan^{-1}\left[\frac{1-(T+\frac{1}{4})^{1/2}}{(T-\frac{1}{4})^{1/2}}\right] = \tfrac{1}{4}\pi + n\pi \tag{28}$$

for integer n. Eq. (28) gives an increasing series $(T_n^{R_1})_{n\geq 0}$ of successive positions of a cusp. When centred around the point $T_\mathrm{p} = 1.3529\ldots$, and given a parameter value R_1, parameter R_2 and scaling factor α can be determined under which the map is self-similar. An example is given in Fig. 8.

4. Discussion and conclusion

The dynamical system analysed in this paper is a simple, energetically closed, model for convection [14], describing the motion in a vertical plane of the centre-of-mass of a fluid contained in a box and heated from below. Through a translation and reorientation, the equations can be identified with those of Lorenz [12], but the present choice conforms with the common notion that gravity points downwards. This model is analysed when the Prandtl-and Rayleigh-numbers $\sigma, B \to \infty$, while $R \equiv B/\sigma^2$. The resulting set of ODEs are termed the diffusionless Lorenz equations (DLE).

The limit $\sigma \to \infty$ implies that friction is infinitely more important than (thermal) diffusion, resulting in the vanishing of terms which represent diffusion; the input of energy is balanced only by dissipation of momentum. This has two profound implications, the DLE become a one-parameter model (whereas the Lorenz model has three) and the familiar diffusive equilibrium ceases to exist. This simplification of the Lorenz equations gives a condensation of its dynamics to processes involving the convective stationary states $C^\pm$ only, which can be readily investigated in the one-dimensional parameter space.

There are several parallels between this and earlier studies, and we will try to clarify these relations here. The heteroclinic orbits found in the DLE were earlier reported by Sparrow [18, Chapter 8] and Glendinning

and Sparrow [7]. However, the heteroclinic Shil'nikov orbits found in these latter studies were produced by a homoclinic explosion, or Lorenz bifurcation, involving the stationary point at the origin which is not the case here. All orbits found in the DLE originate and terminate in heteroclinic Shil'nikov bifurcations, except for the one termed symmetric principal branch, which originates in a heteroclinic bifurcation but extends in parameter space towards positive infinity. The stable limit cycles which exists for $R \to \infty$, originate near $R \approx 1$ by the simplest possible heteroclinic bifurcation, involving $C^{\pm}$. This in contrast to the Lorenz model [6] where they emerge in a homoclinic bifurcation involving the stationary point at the origin. An exact solution for periodic motion at $R \to \infty$ has been proposed in terms of the second Painlevé transcendent.

In parameter space, the orbits approach a heteroclinic bifurcation on a spirally-shaped curve in the amplitude–parameter space [6]. Almost all numerically observed behaviour is due to bifurcations on the outermost branch of these Shil'nikov curves, and all its features, being the lower limits of the Shil'nikov bifurcations in parameter space, symmetry breaking and period-doubling cascades to chaos, can be explored in parameter space for the case $0 < R \ll 1$ with an even simpler representation of the dynamics: its reduction to an analytic map. Lorenz [12] obtained the single-cusped 'tent-map', relating the amplitude of one oscillatory cycle to that of the next. The difference equation for this tent-map is defined graphically rather than analytically as we do here (see, e.g. ref. [15] for recent research on the Lorenz equations along these lines). In another publication [13], Lorenz retrieved a multi-cusped map. An analytic map, with similar such results, is presented here.

This map proves to be self-similar, which enables us to make predictions of its behaviour as $R \downarrow 0$. With infinitely many bifurcations squeezed into infinitely thin regions as R approaches zero, makes this limit rather cumbersome to consider in any other fashion.

An elaborate implicit, analytical map based on the full Lorenz equations was derived earlier, under more general circumstances, by Fowler and McGuinness [4,5]. However, the derivation presented here leads to an explicit map and is much simpler to establish due to the simplified nature of the DLE. The cusps in the Fowler and McGuinness map are associated with a trajectory which lies on the stable manifold of the diffusive equilibrium, the origin in the original Lorenz model, and thus with the appearance in the system of homoclinic orbits. The analogue of this trajectory in the DLE, where the diffusive equilibrium is absent, is one which coincides with the z-axis. In the equivalent pendulum analogy, the cusps physically correspond to the unlikely event that the pendulum ends up exactly in the upright, inverted, position with its radius constantly increasing due to the forcing. It will take an infinite amount of time for an instability to grow large enough to overturn the pendulum. The finite height of the cusps of the Fowler and McGuinness map [4,5] can be explained using this analogy. In the presence of diffusion, modelled proportional to the amplitude of the variables, the amplitude of z will continue to grow when the pendulum is inverted, until diffusion balances the forcing exactly and further growth of z is halted. Apparently the presence of the diffusive equilibrium is not of importance for the occurrence of multiple cusps, but merely affects their height.

Acknowledgements

We thank Dr. C. Sparrow for directing our attention to Glendinning and Sparrow [6] and we acknowledge the help of Drs. A. Doelman and F. Verhulst. We are grateful for discussions with Drs. G.P. Schramkowski and J.T.F. Zimmerman and we thank the (anonymous) referees for their useful remarks and suggestions. The investigations were supported by the Netherlands Geosciences Foundation (GOA) with financial aid from the Netherlands Organization for Scientific Research (NWO). This is the contribution No. 3370 from the Netherlands Institute for Sea Research.

Appendix A. Approximate solution for $R \gg 1$

When $R \gg 1$, Eqs. (2a)–(2c) feature a simple periodic motion (Fig. 1a). This two-lobed stable periodic state can be characterized by rescaling (2a)–(2c) with $\delta = R^{-1/2}$:

$$x \to \delta^{-1}x, \qquad (y, z) \to \delta^{-2}(y, z), \qquad t \to \delta t$$

and results in a weakly-forced and weakly-damped version of (2a)–(2c),

$$\dot{x} = -y - \delta x, \tag{A.1a}$$

$$\dot{y} = -xz, \tag{A.1b}$$

$$\dot{z} = xy + \delta. \tag{A.1c}$$

An approximate solution in terms of an asymptotic series in the small parameter δ can be obtained along the lines set out by Robbins [16]. By substituting a formal expansion $(x, y, z) = (x_0, y_0, z_0) + \delta(x_1, y_1, z_1) + \mathrm{O}(\delta^2)$, we obtain in lowest order:

$$\dot{x}_0 = -y_0, \tag{A.2a}$$

$$\dot{y}_0 = -x_0 z_0, \tag{A.2b}$$

$$\dot{z}_0 = x_0 y_0. \tag{A.2c}$$

The distance of the centre-of-mass to the geometric centre (the length of the equivalent pendulum) b and the total amount of energy, being the sum of kinetic energy and potential energy d, are conserved. Eqs. (A.2a)–(A.2c) are solved by [16]:

$$x_0(t) = a \,\mathrm{cn}\, u, \tag{A.3a}$$

$$y_0(t) = -ab^{1/2} \,\mathrm{sn}\, u \,\mathrm{dn}\, u \tag{A.3b}$$

$$z_0(t) = b(1 - 2\,\mathrm{dn}^2\, u). \tag{A.3c}$$

Here $u = b^{1/2}t + u_0$ denotes the phase and

$$a = 2(b + d)^{1/2}, \tag{A.4}$$

the amplitude, while sn, cn and dn denote the bivariate Jacobi elliptic functions, whose dependence on the parameter is suppressed here. These functions are $4K$-periodic, with $K \equiv K(m)$ denoting the complete elliptic integral of the first kind of modulus

$$m \equiv \frac{a^2}{4b}. \tag{A.5}$$

A third integration constant, u_0, determines their solutions up to an arbitrary time shift. For the original, slightly *viscous* set of equations (A.1a)–(A.1c), irrespective of the precise initial conditions, always one *particular* zeroth-order periodic orbit is reached. This orbit can be determined without recourse to the higher order solution by simply requiring that it is such that there is no net change in the length nor any net gain or loss of energy over one cycle. Since, from (A.1a)–(A.1c),

$$\frac{\mathrm{d}}{\mathrm{d}t}(y^2 + z^2) = \delta z, \qquad \frac{\mathrm{d}}{\mathrm{d}t}(\tfrac{1}{2}x^2 + z) = \delta(1 - x^2),$$

a periodic solution will satisfy, to $O(\delta)$

$$\langle z_0 \rangle = 0 \quad \text{and} \quad \langle 1 - x_0^2 \rangle = 0,$$

where

$$\langle () \rangle = \frac{1}{2K} \int_0^{2K} () \, \mathrm{d}u$$

denotes a phase-average over the period of the squared Jacobi elliptic function $\mathrm{dn}^2 u$. Since the complete elliptic integral of the second kind, $E \equiv E(m) = \int_0^K \mathrm{dn}^2 u \, \mathrm{d}u$, the modulus m is, by the first requirement, on substituting (A.3c), determined as the root of

$$2E(m) = K(m), \tag{A.6}$$

or (numerically) $m \approx 0.826115$. The second requirement, with (A.3a), yields

$$\frac{a^2}{K} \int_0^K \mathrm{cn}^2 u \, \mathrm{d}u = 1, \tag{A.7}$$

where the integration can be performed on $[0, K]$ considering the periodicity of cn. Together with another representation of $E = (1 - m)K + m \int_0^K \mathrm{cn}^2 u \, \mathrm{d}u$, replacing E from (A.6), this gives

$$a^2 = \frac{2m}{2m - 1}. \tag{A.8}$$

The latter equation, combined with the definition of m, (A.5), determines the length of the equivalent pendulum:

$$b = \frac{1}{2(2m - 1)} \approx 0.766601, \tag{A.9}$$

which is reached asymptotically, regardless of the initial conditions. Hence, using (A.4) the total energy of the asymptotic motion is $d = \frac{1}{2}$. Finally, x ($\propto \mathrm{cn}\, u$) is $4K$ periodic, whence the period of each oscillation is $T = 4K/b^{1/2} \approx 10.6038$.

Substituting the original scale for t used in Eqs. (1a)–(1c) we obtain a relation between the period T of the motion and the flux-Rayleigh number B: $T \approx 10.6\, B^{-1/2}$. A characteristic period of thermal convection in a very viscous fluid, corresponding to a high Prandtl-number, can also be determined numerically [2] and experimentally [3]. The analytical result agrees fairly well with these methods, which show that the dimensionless characteristic period depends on the $-\frac{1}{2}$-power of the flux-Rayleigh number, with proportionality constants 14 and 12.4, respectively.

References

[1] E. Doedel, AUTO: Software for Continuation and Bifurcation Problems in Ordinary Differential Equations, Cornell University Press, Ithaca, NY, 1986.
[2] T.D. Foster, Intermittent convection, Geophys. Fluid Dyn. 2 (1971) 201–217.
[3] T.D. Foster, S. Waller, Experiments on convection at very high Rayleigh numbers, Phys. Fluids 28 (1985) 455–461.
[4] A.C. Fowler, M.J. McGuinness, A description of the Lorenz attractor at high Prandtl number, Physica D 5 (1982) 149–182.
[5] A.C. Fowler, M.J. McGuinness, Hysteresis, period doubling, and intermittency at high Prandtl number in the Lorenz equations, Stud. Appl. Math. 69 (1983) 99–126.
[6] P. Glendinning, C. Sparrow, Local and global behavior near homoclinic orbits, J. Stat. Phys. 35 (1984) 645–697.
[7] P. Glendinning, C. Sparrow, T-points: a codimension two heteroclinic bifurcation, J. Stat. Phys. 43 (1986) 479–488.
[8] J. Guckenheimer, P. Holmes, Nonlinear Oscillations, Dynamical Systems, and Bifurcations of Vector Fields, Springer, Berlin, 1983.
[9] E.L. Ince, Ordinary Differential Equations, Dover, New York, 1956.

[10] M. Kolář, G. Gumbs, Theory for the experimental observation of chaos in a rotating waterwheel, Phys. Rev. A 45 (1992) 626–637.
[11] Y.A. Kuznetsov, Elements of Applied Bifurcation Theory, Springer, Berlin, 1995.
[12] E.N. Lorenz, Deterministic non-periodic flow, J. Atm. Sci. 20 (1963) 130–141.
[13] E.N. Lorenz, On the prevalence of aperiodicity in simple systems, in: M. Grmela, J.E. Marsden (eds.), Global Analysis, Springer, Berlin, 1979, pp. 53–75.
[14] L.R.M. Maas, A simple model for the three-dimensional thermally and wind-driven ocean circulation, Tellus A 46 (1994) 671–680.
[15] O. Michielin, P.E. Phillipson, Map dynamics study of the Lorenz equations, Inter. J. Bif. Chaos 7 (1997) 373–382.
[16] K.A. Robbins, Periodic solutions and bifurcation structure at high R in the Lorenz model, SIAM J. Appl. Math. 36 (1979) 457–472.
[17] T. Shimizu, Analytic form of the simplest limit cycle in the Lorenz model, Physica A 97 (1979) 383–398.
[18] C.T. Sparrow, The Lorenz Equations: Bifurcations, Chaos and Strange Attractors, Springer, Berlin, 1982.
[19] J.C. Sprott, Some simple chaotic flows, Phys. Rev. E 50 (1994) 647–650.
[20] M. Tabor, Modern dynamics and classical analysis, Nature 310 (1984) 277–282.
[21] M. Tabor, Chaos and Integrability in Nonlinear Dynamics: An Introduction, Wiley, New York, 1989.
[22] S. Wiggins, Introduction to Applied Nonlinear Dynamical Systems and Chaos, Springer, Berlin, 1991.